

This is a repository copy of *Plasma-Induced Interfacial Processes in Metal Halides FTIR Gas Cell Windows*.

White Rose Research Online URL for this paper:

<https://eprints.whiterose.ac.uk/207536/>

Version: Published Version

Article:

Olenik, Jaka, Shvalya, Vasyl, Modic, Martina et al. (4 more authors) (2023) Plasma-Induced Interfacial Processes in Metal Halides FTIR Gas Cell Windows. *Journal of Analysis and Testing*. pp. 392-404. ISSN 2509-4696

<https://doi.org/10.1007/s41664-023-00274-y>

Reuse

This article is distributed under the terms of the Creative Commons Attribution (CC BY) licence. This licence allows you to distribute, remix, tweak, and build upon the work, even commercially, as long as you credit the authors for the original work. More information and the full terms of the licence here:

<https://creativecommons.org/licenses/>

Takedown

If you consider content in White Rose Research Online to be in breach of UK law, please notify us by emailing eprints@whiterose.ac.uk including the URL of the record and the reason for the withdrawal request.



Plasma-Induced Interfacial Processes in Metal Halides FTIR Gas Cell Windows

Jaka Olenik¹ · Vasyly Shvalya² · Martina Modic² · Jernej Ekar^{3,4} · Janez Kovac³ · Uroš Cvelbar² · James L. Walsh¹

Received: 1 August 2023 / Accepted: 16 October 2023 / Published online: 12 December 2023
© The Author(s) 2023

Abstract

Fourier transform infrared spectroscopy (FTIR) is one of the most widely used vibrational diagnostic techniques to investigate gas-phase reactive oxygen and nitrogen species (RONS). However, the technique carries intrinsic challenges, particularly in relation to interfering peaks in the spectral data. This study explores the interfacial processes that occur when reactive oxygen and nitrogen species generated by a non-equilibrium air plasma interact with the metal halide windows of an FTIR gas cell, leading to the appearance and evolution of spurious absorption peaks which complicate spectral interpretation. Raman spectroscopy, X-ray photoelectron spectroscopy, time of flight secondary ion mass spectrometry and attenuated total reflectance-FTIR spectroscopy were used to elucidate the origin of spurious absorption peaks spanning the 1400–1300 cm⁻¹ spectral range as a result of KBr exposure to plasma generated species. It was found that plasma exposed KBr contained a lower atomic fraction of Br which was replaced by the NO₃ nitrate group, the main absorbance peak of which progressively evolved with plasma exposure and affected the window transparency over the corresponding FTIR region. A correlation was revealed between KNO₃ formation, plasma power and exposure time to a growth and change in molecular vibrational energies corresponding to asymmetric NO₃ stretching vibrations in the KNO₃ structure.

Keywords Cold atmospheric-pressure plasma · Gas-phase FTIR · RONS · IR windows · Surface functionalisation · KBr

1 Introduction

Within the past decade, research into cold atmospheric-pressure plasma (CAP) has experienced a renaissance driven by its many diverse applications that span the fields of medicine, materials science, and agriculture. For example, CAP has been shown to be extremely efficient in enhancing the germination rate of seeds [1], in the decontamination of food and food processing surfaces [2], in the degradation of carcinogenic mycotoxins [3], and in the production of

novel organic and inorganic nanomaterials with improved optical, magnetic and electrical performance [4, 5]. Non-equilibrium, or cold, atmospheric pressure plasmas possess unique physicochemical properties and typically comprise of short- and long-lived reactive chemical species accompanied by energetic electrons, ions, intense electric fields and UV radiation [6]. In many CAP applications, it is the reactive chemical species produced by the discharge that are of paramount importance; therefore, qualitative and quantitative assessment of these species is vital to understand the underpinning processes that drive the interaction between CAP and external matter. There are many different emission and absorption-based spectroscopic techniques that can be used to probe plasma-generated reactive chemical species, among which Fourier-transform infrared (FTIR) spectroscopy stands out for the evaluation of typical long-lived reactive oxygen and nitrogen species (RONS) created by CAP [7, 8].

By utilising FTIR with a gas cell, it is possible to assess the dynamic vibrational behaviour of gaseous molecules and functional groups. When plasma is generated in ambient air,

✉ James L. Walsh
james.l.walsh@york.ac.uk

¹ York Plasma Institute, School of Physics, Engineering and Technology, University of York, York YO10 5DD, UK

² Department for Gaseous Electronics F6, Jozef Stefan Institute, 1000 Ljubljana, Slovenia

³ Department of Surface Engineering F4, Jozef Stefan Institute, 1000 Ljubljana, Slovenia

⁴ Jozef Stefan International Postgraduate School, 1000 Ljubljana, Slovenia

these RONS include O_3 , NO, N_2O , NO_2 , NO_3 , and N_2O_5 , which typically appear within the sub- 2000 cm^{-1} IR region [9, 10]. The quantitative and qualitative analyses of these species using FTIR is common practice, with the approach necessitating the use of metal halide IR transparent windows such as potassium bromide (KBr), barium fluoride (BaF_2), calcium fluoride (CaF_2), thallium bromoiodide (KRS-5), cadmium telluride (CdTe), zinc selenide (ZnSe), and others, to trap gaseous species in the cell for assessment [11].

A number of past studies have employed FTIR gas-phase spectroscopy in CAP research. Sivachandiran et al. used FTIR gas-phase spectroscopy with a 10-m-long path cell to monitor the discharge chemistry used to chemically activate water for enhanced seed germination and plant growth [12]. Likewise, Reuter et al. adopted the technique to perform H_2O_2 measurements on the kiNPen plasma jet device to investigate skin cell treatment [13]. The approach was also used to reveal differences in transmission spectra between the inlet and outlet of a plasma discharge generated within a porous ceramic reactor for the decomposition of volatile organic compounds such as ethylene [14]. An FTIR system equipped with a short-path gas cell capped with KBr windows was also employed to identify different regimes of operation during plasma catalytic ammonia synthesis [15]. Furthermore, the technique is used widely for the quantification of key RONS generated in air-based CAP discharges [16], thus the approach facilitates an insight into the plasma chemistry and its evolution over time, including important phenomena such as the complex time- and power-dependent interplay between O_3 and NO_2 [17].

Despite all of the benefits that the FTIR technique offers for the assessment of plasma generated RONS, there exists the potential for the aggressive chemical environment created by the plasma to negatively affect the measurement, giving rise to artefacts in the spectra that interfere with data interpretation and may even persist long after the plasma has been extinguished. In essence, our preliminary investigations have revealed that the background IR spectrum of a gas cell employing KBr windows is irrevocably altered following exposure to CAP generated RONS. A broad, unknown and unexpected peak was observed in the IR spectral region between 1300 and 1400 cm^{-1} when investigating CAP generated in ambient air using FTIR gas analysis.

To elucidate the origin of the unidentified peak, this study explored the interaction between KBr and the RONS generated by an air-fed CAP. Changes to the surface composition were characterised by X-ray photoelectron spectroscopy (XPS), attenuated total reflectance (ATR) FTIR spectroscopy, and Raman spectroscopy. The results showed that RONS generated by the plasma react with K to form KNO_3 on the surface of the windows, leading to a permanent change in the surface composition of the KBr windows. This KBr functionalisation manifests itself as a broad absorption

peak spanning the 1300 – 1400 cm^{-1} range, which grows in magnitude with the duration and intensity of plasma exposure, and thus cannot easily be removed by background subtraction and must be carefully considered when interpreting FTIR data of CAP generated RONS.

2 Methods and Experimental Setup

2.1 KBr Windows

Surface analysis was performed on KBr windows (160 – 1320 , PIKE Technologies) that were included in a gas cell kit (Short-Path HT Gas Cell, 100 mm path length, 162 – 2200 , PIKE Technologies). The windows were used for initial surface analysis, while KBr pellets were prepared for more in-depth analysis. These pellets were prepared by pressing 100 mg of KBr powder into a pellet shape (diameter: 6 mm , height: 1.3 mm).

2.2 CAP Setup

Both windows and pellets were exposed to plasma using a custom-built capacitively coupled surface barrier discharge (SBD) system, described in previous CAP studies [18–21]. Briefly, the SBD system consisted of a quartz dielectric glass sheet sandwiched between a powered electrode and a hexagonal mesh ground electrode. When exposing KBr pellets, the SBD electrode was enclosed in a box with a similar volume to the short-pass gas cell used in FTIR measurements, to mimic the standard method of measuring RONS with FTIR gas cell as seen in Fig. 1a. Pellets were positioned flat on a glass slide in the middle of the SDB enclosure, exposing one side to the plasma at a distance of 60 mm from SBD ground electrode. The samples were treated for varying lengths of time (30 , 60 , 120 , 240 and 480 s) under both low-power (2.8 W) and high-power (7.2 W) mode, with a frequency of 14 kHz . The two operating power conditions were chosen based on the access to the two distinct operating modes of an SBD [17, 18], where low-power operation facilitates ROS production and high-power operation facilitates RNS production.

2.3 Plasma and Gas Phase Diagnostics

To understand the formation processes giving rise to long-lived RONS in the effluent of the discharge, the nature of excited species present within the discharge layer and the rotational and vibrational temperature of the plasma were assessed using optical emission spectroscopy (OES). The OES system utilised a fiber optic coupled spectrograph (Shamrock SR500i-D2-R, Andor) equipped with an intensified CCD camera (iStar 334T CCD, DH334T-18U-O3,

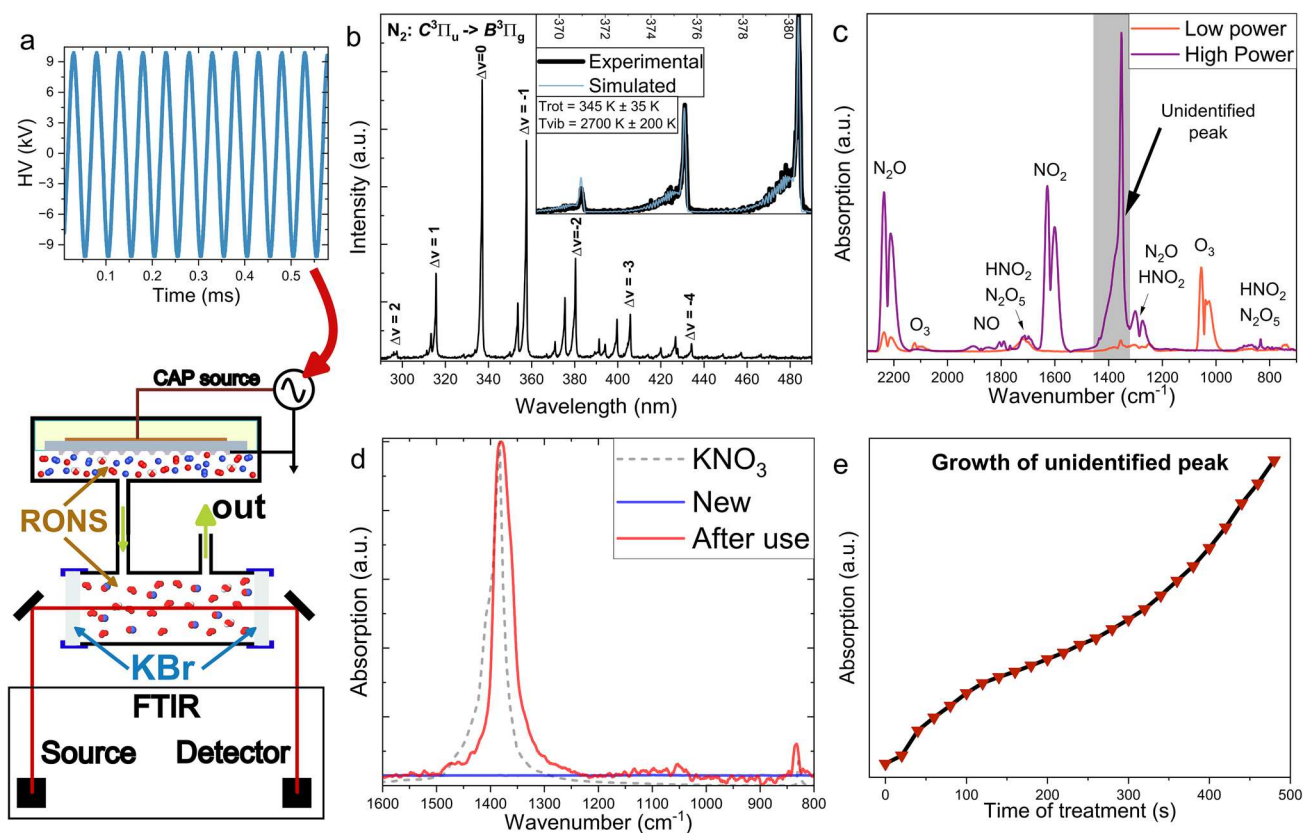


Fig. 1 **a** Schematic of the FTIR system used for plasma gas analysis with a typical voltage waveform. **b** OES spectra of SBD plasma discharge operating under high-power conditions, inset shows high-resolution data of the second positive nitrogen system transition ($\Delta v = -2$) overlaid with a simulated profile at $T_{\text{rot}} = 345 \pm 35$ K and $T_{\text{vib}} = 2700 \pm 200$ K. **c** Gas composition of the long-lived plasma spe-

cies showing an unidentified peak at 1380 cm^{-1} . **d** ATR-FTIR spectra of KBr windows before and after plasma exposure with comparative data from KNO_3 obtained from the NIST reference database [25]. **e** Growth curve of the unidentified peak at 1380 cm^{-1} with plasma exposure time

Andor). To gain an appreciation of the excited states within the plasma, light emitted from the plasma was recorded across a broad spectral range of 200–800 nm with a 300 lines/mm grating. The high-resolution spectral data necessary for temperature measurements were acquired from 360 to 385 nm with a 1200 lines/mm grating.

To assess the gas phase effluent of the plasma, a FTIR spectrometer (Frontier IR, PerkinElmer) equipped with the described 100-mm-path length high-throughput gas cell was used. The SBD enclosure was connected to the gas cell with a 50-cm long tube with an outer diameter of 8 mm. To promote the flow of the RONS into the cell, 1 slm of dry air was pumped through the SBD enclosure. The measurements were taken at room temperature and the spectra were acquired across the range of $4000\text{--}400 \text{ cm}^{-1}$ with a resolution of 1 cm^{-1} and an averaging over 10 scans.

2.4 XPS Analysis

The surface atomic composition and bonding environment of KBr was examined using X-ray photoelectron spectroscopy (PHI-TFA XPS, Physical Electronics Inc). The spectrometer was equipped with an Al-monochromatic X-ray source operating at a pass energy of 1486.6 eV and featured active surface charge neutralisation. The data was acquired under ultra-high vacuum conditions (greater than 1×10^{-8} Pa) to ensure minimal surface contamination. Spectra were corrected to give the adventitious C 1 s spectral component (C–C, C–H) binding energy of 284.7 eV and analysed for elemental composition using the Multipack software. The peaks were further deconvoluted using a Gaussian fitting function and Shirley-type background subtraction, performed using the OriginLab software, without considering any tailing function in the peak fitting procedure.

2.5 FTIR-ATR Analysis

The vibrational energies of bonds formed at the molecular level in KBr were determined using FTIR-ATR measurements. These measurements were taken at room temperature using an FTIR instrument (Frontier IR, L1280018, PerkinElmer) combined with an ATR module (UATR Accessory for Frontier, KRS-5, L1280304, PerkinElmer) across the spectral range of 4000–400 cm^{-1} with a resolution of 1 cm^{-1} and an averaging over 10 scans.

2.6 Raman Analysis

The Raman Analysis was conducted using a confocal Raman spectrometer (NTEGRA Spectra II, NT-MDT Spectrum Instruments) operating in a back-scattered geometry. The sample was illuminated with a monochromatic laser operating at a wavelength of 633 nm, which was focused on the sample surface by applying a 60 \times magnifying objective lens. To acquire the spectra, the samples were exposed to the laser beam for 10 s, with 5-times accumulation. This process was repeated at five different regions of the sample surface to ensure the reproducibility of the results. The obtained spectra were then baseline subtracted, smoothed and normalised to form the final experimental data.

2.7 ToF-SIMS Analysis

Elemental and isotope surface analysis was made using a ToF-SIMS instrument (TOF.SIMS 5, IONTOF). Bi_3^+ primary ions with an energy of 30 keV and a current between 1.0 and 1.2 pA were used as the analysis beam [22]. The Bi_3^+ primary ion beam was pulsed with a pulse length of 6.5 ns, resulting in a mass resolution $m/\Delta m$ between 2000 and 6000. Analyses were done over a 100 $\mu\text{m} \times 100 \mu\text{m}$ area and the analysis time for mass spectra measurements was 60 s. With the settings used, the analysed depth was about 2 nm, and the lateral resolution was approximately 5 μm . Depth profiling was performed in a dual-beam depth profiling mode. Sputtering was done with the 1 keV Cs^+ ion beam with a current of approximately 60 nA. The depth-profiling crater was sputtered with the Cs^+ ions over a 400 $\mu\text{m} \times 400 \mu\text{m}$ area while analysis was performed in the centre of the crater with the Bi_3^+ ions over the 100 $\mu\text{m} \times 100 \mu\text{m}$ area. Secondary ions were analysed during both measurement of mass spectra and depth profiling over the m/z range from 0 to 850. During both types of analyses, low-energy electron flood gun was also applied for the neutralisation of the charge build-up due to the insulating nature of the samples. Pressure during measurements was in the range of 10^{-7} Pa.

3 Results and Discussion

3.1 CAP generation and Characterisation

On application of a sufficiently high voltage to the SBD electrode (Fig. 1a), gas breakdown was observed to occur along the edges of the grounded electrode, which spread across the dielectric surface. OES was used to identify excited states within the discharge (Fig. 1b) and showed the characteristic emission bands of the Nitrogen second positive system. No emission was observed at 777 nm and 844 nm, indicating an absence of excited atomic oxygen. Using high-resolution OES, the rotational and vibrational temperature of the discharge was assessed via comparison with simulated data at $T_{\text{rot}} = 345 \text{ K} \pm 35 \text{ K}$ and $T_{\text{vib}} = 2700 \text{ K} \pm 200 \text{ K}$, which is in line with previously reported studies employing air CAP generated using the SBD configuration [23].

3.2 Long-Lived Species

Highly reactive species primarily created through electron driven dissociation (e.g., N, O, H and OH) diffuse away from the discharge layer and rapidly react to form a variety of longer-lived RONS, including O_3 , H_2O_2 , NO, and other N_xO_y molecules [24]. FTIR gas phase analysis (Fig. 1c) revealed the composition of the gas phase effluent under low- and high-power modes of operation. Results indicated that under low-power conditions, O_3 was the primary long-lived product, formed through a reaction involving atomic and molecular oxygen (Table 1—reaction R1) [24]. In contrast, under high-power conditions, the gas phase effluent was dominated by N_xO_y species, such as N_2O and NO_2 .

The transition between O_3 -dominated to N_xO_y -dominated RONS composition occurs via a multi-step process and has been widely reported in the literature [17]. First, as the discharge power increases, the rate of thermal decomposition of O_3 increases, resulting in less O_3 . Second, an increased power also results in more NO, which inhibits O_3 production via direct decomposition to O_2 and NO_2 , and through the consumption of O, a key precursor for O_3 formation, described in reactions R2–R4 (Table 1).

Most of the absorption peaks shown in Fig. 1c can be directly linked to RONS widely accepted to be generated by

Table 1 Typical ozone formation and destruction reaction pathways in atmospheric pressure air plasma [24] (M represents a non-reacting third body)

No.	Reaction
R1	$\text{O} + \text{O}_2 + \text{M} \rightarrow \text{O}_3 + \text{M}$
R2	$\text{NO} + \text{O}_3 \rightarrow \text{NO}_2 + \text{O}_2$
R3	$\text{NO}_2 + \text{O}_3 \rightarrow \text{NO}_3 + \text{O}_2$
R4	$\text{NO} + \text{O} + \text{M} \rightarrow \text{NO}_2 + \text{M}$

CAP created in ambient air under different power regimes [16]. The exception is the significant absorption peak observed at $\sim 1380\text{ cm}^{-1}$ (shaded grey), which does not relate to known RONS produced by CAP. Following exposure to CAP generated RONS, the absorption peak at 1380 cm^{-1} remains indefinitely (Fig. 1d) despite flushing the cell with filtered air for many minutes following exposure. Also shown in Fig. 1d is the infrared spectrum of KNO_3 retrieved from the NIST spectral database [25], providing a clear indication that the unexpected peak is a likely result of interactions between plasma generated RONS and the KBr windows of the gas cell. Notably, further exposure of the KBr windows to RONS leads to further non-linear growth of the 1380 cm^{-1} absorption peak (Fig. 1e), meaning that the peak cannot easily be removed using background subtraction methods.

3.3 XPS Surface Analysis of KBr Samples

To understand the origin of the 1380 cm^{-1} absorption peak observed in Fig. 1, multiple surface analysis techniques were used. XPS was adopted to determine compositional changes to the surface of exposed KBr (Fig. 2). The control sample shows the typical spin–orbit splitting K2p (293 eV) and Br3d (69 eV) with an atomic concentration ratio close to 1:1 (Table 2). Moreover, carbon (C1s—284.5 eV) and oxygen (O1s—532 eV) peaks were detected, indicating contamination due to absorption of impurities from the ambient air [26]. No nitrogen was found on the freshly prepared KBr pellet (Fig. 2a). In contrast, the samples exposed to low-power plasma (Fig. 2b) and high-power plasma (Fig. 2c) for the same duration (480 s) show a clearly visible nitrogen N1s peak (407 eV) and a slightly increased atomic oxygen content. Interestingly, the K/Br atomic ratio of the

plasma-exposed samples deviates from that of the control even when the standard error of the instrument is taken into account (Table 2). This could indicate that the anion sublattice is affected by RONS, partially substituted and the surface chemistry of the KBr ionic crystal is changed. In particular, the plasma treatment led to a binding of nitrogen and oxygen on the surface, which was further investigated by deconvolution of the XPS peaks.

The core levels were deconvoluted using the Voigt function to decipher changes in the molecular environments of the Br3d and K2p peaks. In the case of Br (control sample, Fig. 3a), two peaks describing the $3d_{5/2}$ and $3d_{3/2}$ orbital splitting ($\Delta \approx 1.0\text{ eV}$ and area ratio 2:3) were found at the typical positions 68.7 eV and 69.74 eV, respectively [27]. Keeping their positions fixed and taking into account the peak area ratio, the two other exposed samples were investigated (Fig. 3b and c). It can be suggested that the fitted peaks became wider and their intersection is larger when compared with the control sample. These changes could be related to the additional number of chemical bonds contributing to the Br3d peak profile.

Similarly, the XPS profile of the K2p core level ($\Delta \approx 2.8\text{ eV}$ and area ratio 1:2) shows both the $\text{K}2p_{3/2}$ and $\text{K}2p_{1/2}$ components of treated samples to be wider compared to the untreated sample (Fig. 4a), this again

Table 2 XPS surface elemental composition (carbon peak is omitted in component fraction calculations)

Sample	K (%)	Br (%)	N (%)	O (%)	K/Br
Control	40.9 ± 0.3	41.0 ± 0.3	Not detected	18.1 ± 0.3	0.997
Low power	36.7 ± 0.3	33.8 ± 0.3	6.3 ± 0.3	23.2 ± 0.3	1.08
High power	36.8 ± 0.3	31.0 ± 0.3	7.5 ± 0.3	24.7 ± 0.3	1.18

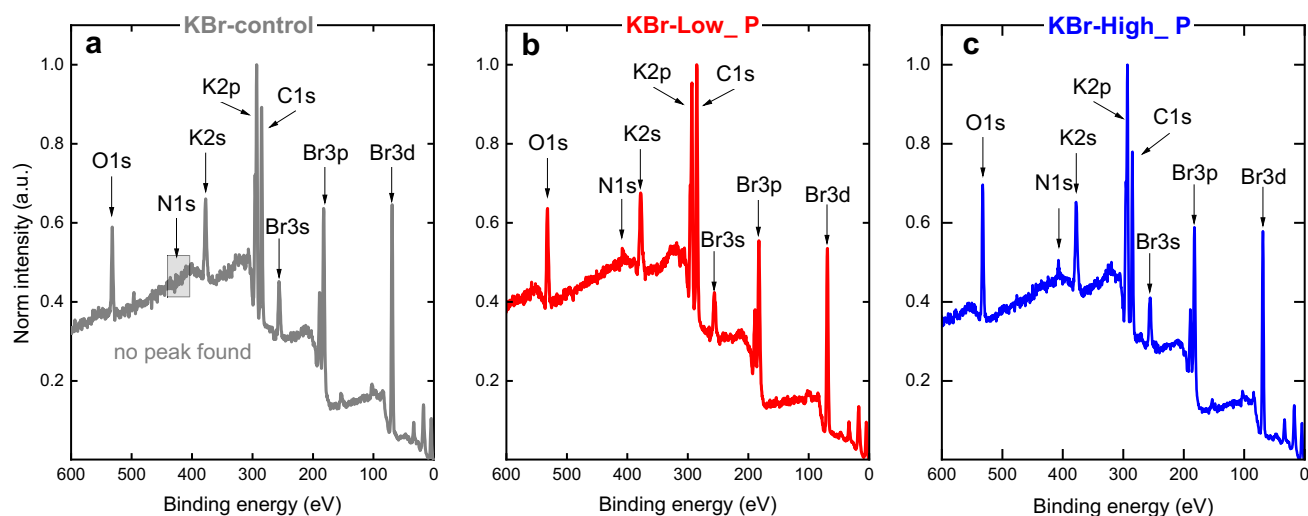


Fig. 2 XPS survey of **a** untreated KBr sample, **b** treated for 480 s with low-power CAP, and **c** treated for 480 s with high-power CAP

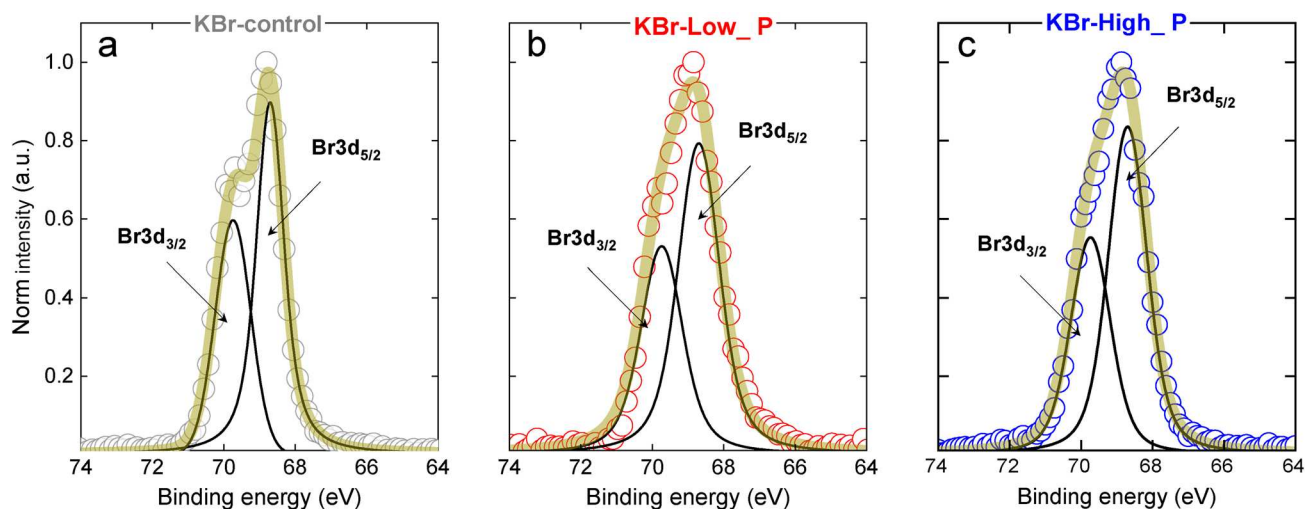


Fig. 3 High-resolution XPS spectra showing Voigt fits of the Br3d core levels for **a** untreated KBr, **b** treated for 480 s with low-power CAP and **c** treated for 480 s with high-power CAP

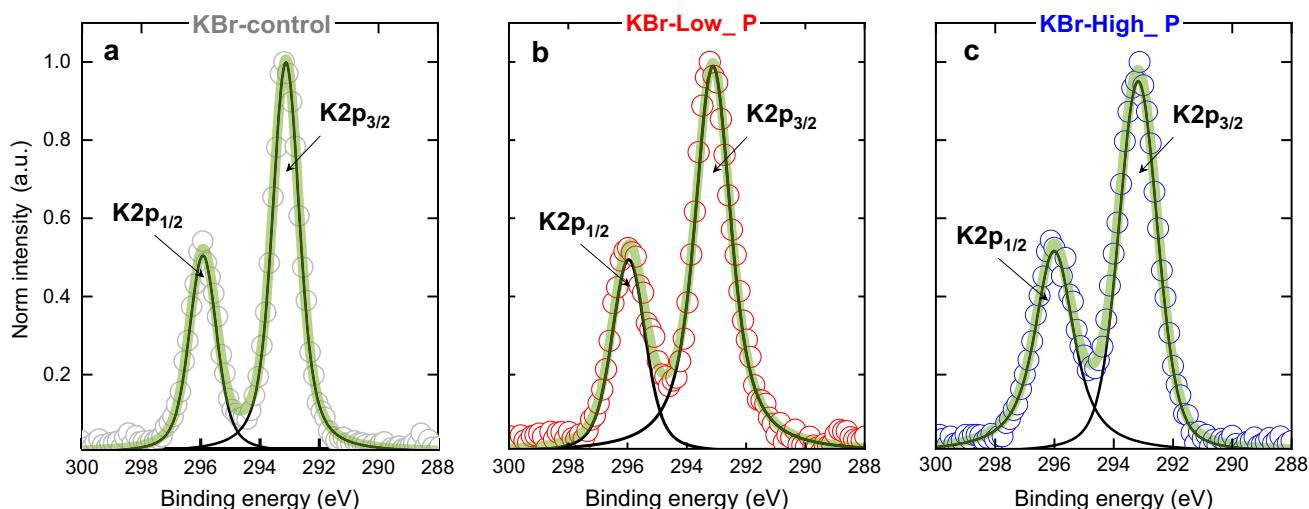


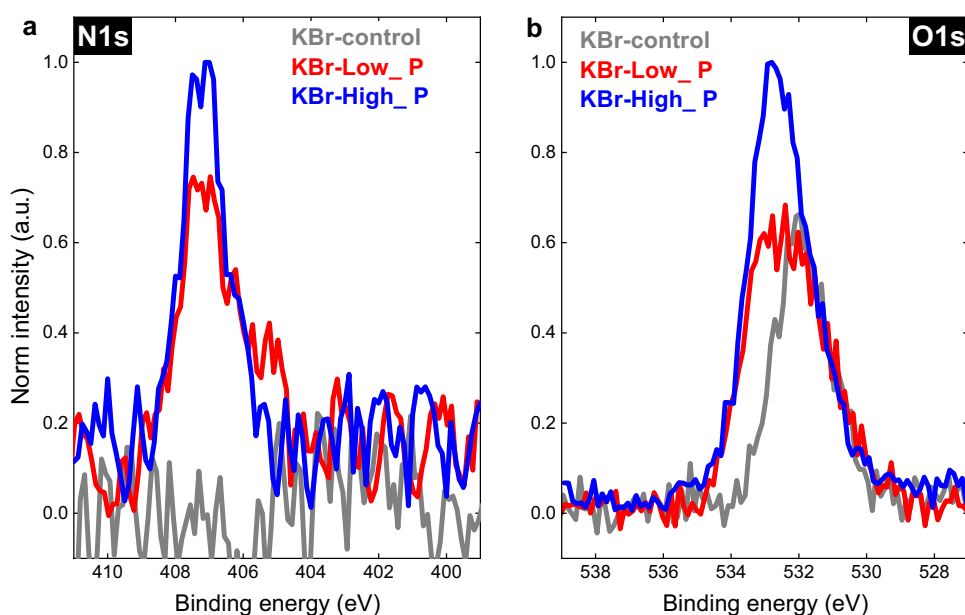
Fig. 4 High-resolution XPS spectra showing Voigt fits of the K2p core levels for **a** untreated KBr, **b** treated for 480 s with low-power CAP and **c** treated for 480 s with high-power CAP

suggests a change in surface chemistry affecting potassium. Furthermore, this assumption could be supported by another observation. Due to the broadening of the peaks, it was not possible to adequately fit the K2p profile using two peaks when strict conditions for position and $K2p_{3/2}/K2p_{1/2}$ ratio were met. In both cases, namely, low-power plasma (Fig. 4b) and high-power plasma (Fig. 4c), the peak area ratio tends to be different from that of the control sample ($K2p_{3/2}/K2p_{1/2} = 2$). At low power, the ratio is 2.45, and at high power it is 1.49. These changes are likely due to the interaction of plasma

generated RONS with the KBr surface, leading to the formation of new chemical bonds and the modification of existing ones.

To investigate the issue further, O1s and N1s were studied for a possible positional cross-check of the NO_x bonds. Prior to analysis, the nitrogen and oxygen regions must first be discussed. In the case of the N1s peak (the normalisation is adjusted to the highest peak), which is not present in the control sample even after a high-resolution scan, the XPS analysis showed a clear contribution of the asymmetric peak at about 407 eV in both cases for low

Fig. 5 High-resolution XPS spectra representing **a** N1s and **b** O1s core levels for untreated KBr (grey), treated with low-power CAP (red) and treated with high-power CAP (blue)



and high-power plasma exposure. However, their asymmetry differs, indicating a possible contribution from more than one oxidation state of nitrogen, especially in the case of the ‘low-P’ plasma (Fig. 5a). As for oxygen (the normalisation is set to the highest peak), which was already present in the control sample because it was exposed to ambient conditions, it is more likely that a broad O1s peak occurs at about 532 eV (Fig. 5b, grey data) due to chemical bonding to carbon (which is also found in all samples and does not differ much, see inset in Fig. 6). After contact with the plasma effluent, the shape of the peak changes as well as its intensity, first broadening (red data in Fig. 5b) and then increasing. This behaviour could be correlated with the changes in the N1s peak, suggesting that the O1s peak is altered by RONS. However, to answer the question about the nature and proportion of the NO_x components, it is sufficient to fit only the N1s profile (the C1s peak has no influence on the profile shape).

After fitting, it is clear that in both cases the contribution of NO_3^- (407.2 eV) dominates (Fig. 6a and b), with an additional portion of NO_2 (405.7 eV) at the surface [28, 29]. The $\text{NO}_3^-/\text{NO}_2$ ratio for the low-power plasma sample is roughly equal to 1.3 and for the high-power plasma it is much higher, being 10.8. The apparent presence of the NO_3^- group and the reduced proportion of Br may indicate that the latter has been partially replaced by a nitrate group and that KNO_3 is formed on the KBr surface after plasma exposure. These changes are likely to be reflected in the transparency of KBr within the mid-range IR spectrum, significantly affecting the properties and performance of the treated material. Thus, these observations are important to explain the origin of unexplained peak during CAP species analysis.

3.4 FTIR-ATR Vibrational Surface Analysis

KBr pellets subjected to a 480 s exposure of CAP showed the formation of several absorption peaks, in clear contrast to the untreated KBr spectra, with the most significant features being found in the $1300\text{--}1500\text{ cm}^{-1}$ region (Fig. 7a), which are accompanied by the appearance of additional smaller peaks spanning the $800\text{--}1800\text{ cm}^{-1}$ spectral region. As shown in Fig. 1, this region is typically used to identify key CAP generated reactive species, including O_3 , NO_2 , HNO_3 and HNO_2 . Comparing Fig. 7a with the data available in the literature indicates the shape of the two modified curves (red and blue) are reminiscent of the NO_3^- anion with ^{14}N and ^{15}N isotopes, whose IR modes also populate a similar wavelength span [30–34].

Since the grey shaded areas are the most affected, they will be the focus of further discussion. The time evolution of this portion of the spectrum (Fig. 7b–c) is quite complex, since the mutual contribution of several modes can be observed regardless of plasma power. Importantly, after prolonged treatment, the low-power (low_P) sample showed the most prominent peak at 1352 cm^{-1} and the largest mode in the high-power (high_P) sample was at 1380 cm^{-1} . To study them in detail, the spectra obtained in both plasma regimes were deconvoluted with the Gaussian function.

The interval of interest ($1500\text{--}1300\text{ cm}^{-1}$, NO_3^- -nitrate anion) includes several interacting IR-active modes with different intensities, most of which are attributed to the vibrational frequencies of either the symmetric stretching of $^{14}\text{N}^{16}\text{O}_3^-$ ($\sim 1380\text{ cm}^{-1}$) and $^{15}\text{N}^{16}\text{O}_3^-$ ($\sim 1350\text{ cm}^{-1}$), or HON bending in HNO_3 (Fig. 8a and b) [33–37]. Through detailed examination of the two peaks, it could be suggested that under high-power conditions at the beginning of the plasma treatment, the IR spectrum of the NO_3^- anion is

Fig. 6 High-resolution XPS spectra representing N1s core levels for **a** treated with low-power CAP and **b** treated with high-power CAP. Inset is a normalised carbon C1s spectra (shift-corrected to 285 eV)

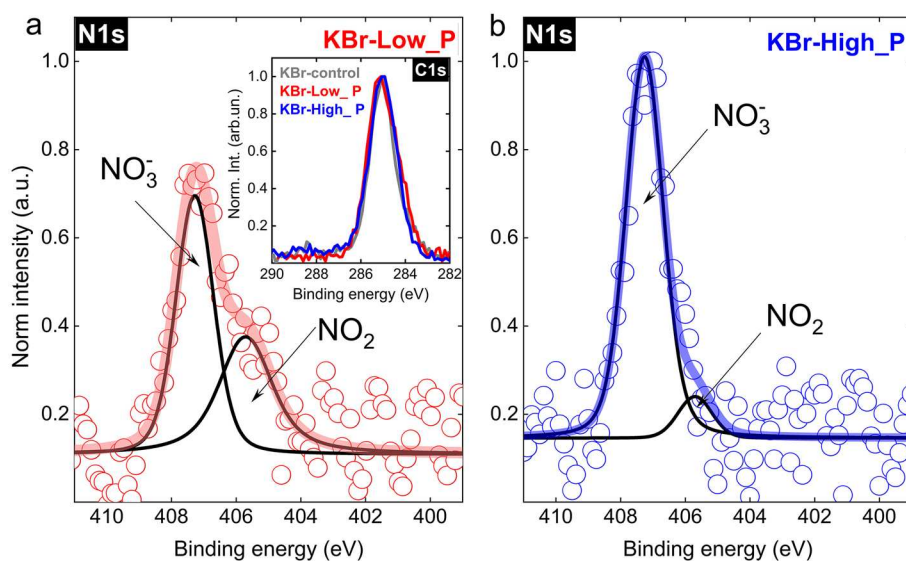


Fig. 7 **a** Wide-range FTIR data of the plasma exposed KBr pellets, time-resolved ATR-FTIR comparison of treated KBr sample with **b** low plasma power and **c** high plasma power

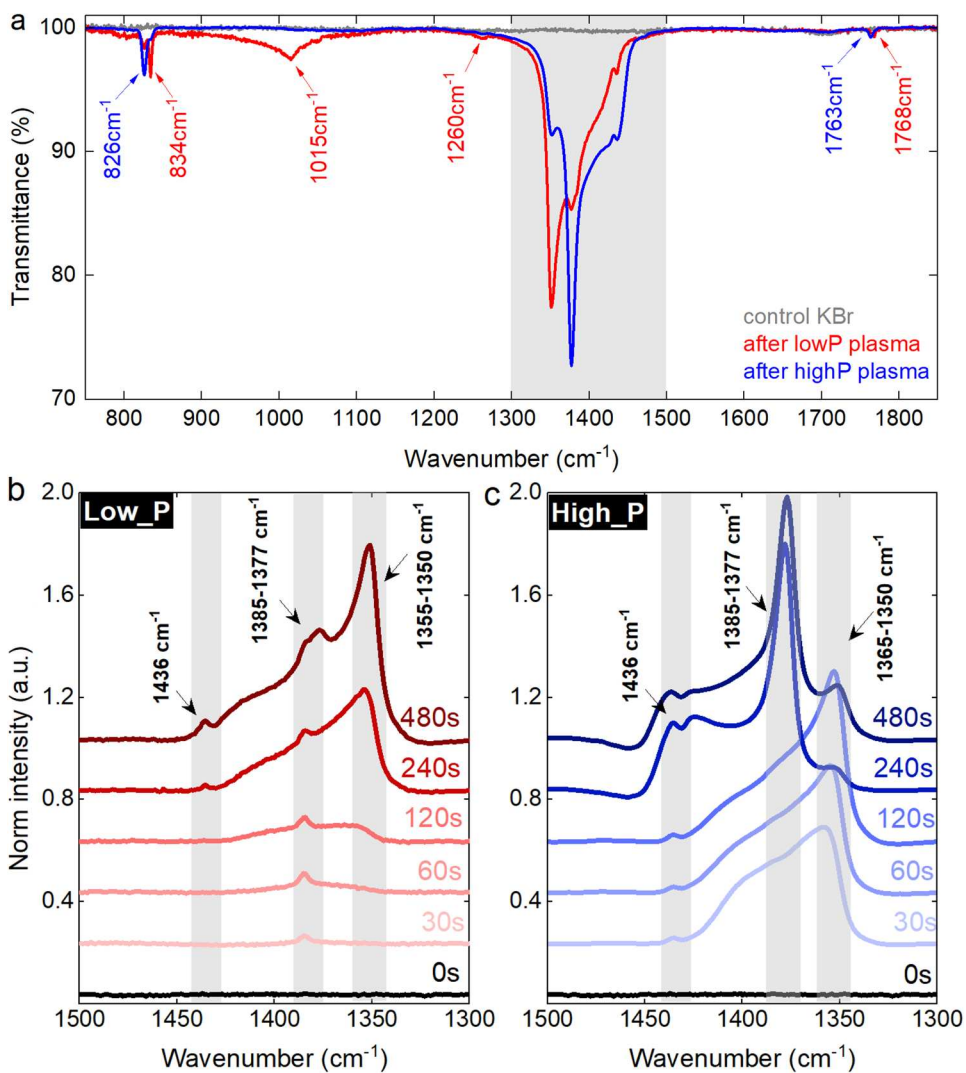
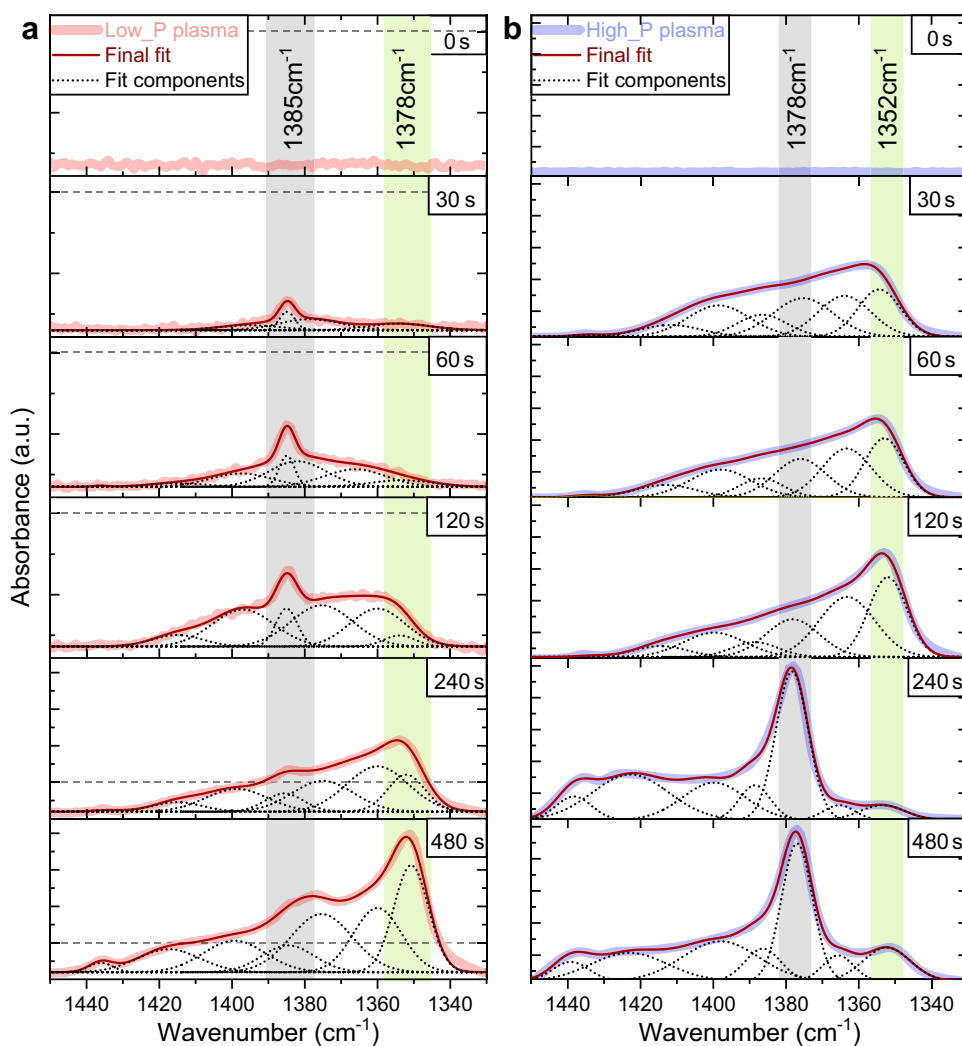


Fig. 8 Deconvoluted FTIR data of treated KBr sample with **a** low plasma power and **b** high plasma power at different lengths of exposure time



overlaid by the contribution of HNO_3 and $^{15}\text{N}^{16}\text{O}_3^-$ which is dominant up to 120 s of exposure. After that and until the end of the treatment, the contribution of the isotope $^{14}\text{N}^{16}\text{O}_3^-$ ($\sim 1380\text{ cm}^{-1}$) in KNO_3 is the strongest. The opposite occurs under low-power conditions, where HNO_3 and $^{15}\text{N}^{16}\text{O}_3^-$ overtake the $^{14}\text{N}^{16}\text{O}_3^-$ ($\sim 1380\text{ cm}^{-1}$) peak under long exposure. In both cases it can be confirmed that the KBr surface is functionalised with a cocktail of different N-containing functional groups, which also leads to the formation of KNO_3 , which is confirmed via Raman analysis in the following section. The small deviation in peak position, observed by comparing the low-power and high-power spectra, could be attributed to the influence of more complex isotopes, including $^{15}\text{N}^{16}\text{O}_3^{18}\text{O}^-$ in the case of the lower standing peak (green shaded area in Fig. 8a and b), and $^{14}\text{N}^{16}\text{O}_3^{18}\text{O}^-$ for the higher standing peak (grey shaded area in Fig. 8a and b) [31]. It is important to note that the origins of the observed stable nitrogen isotopes are assumed to be from the samples being exposed to ambient air where there is an abundance of ^{14}N plus a small amount of ^{15}N

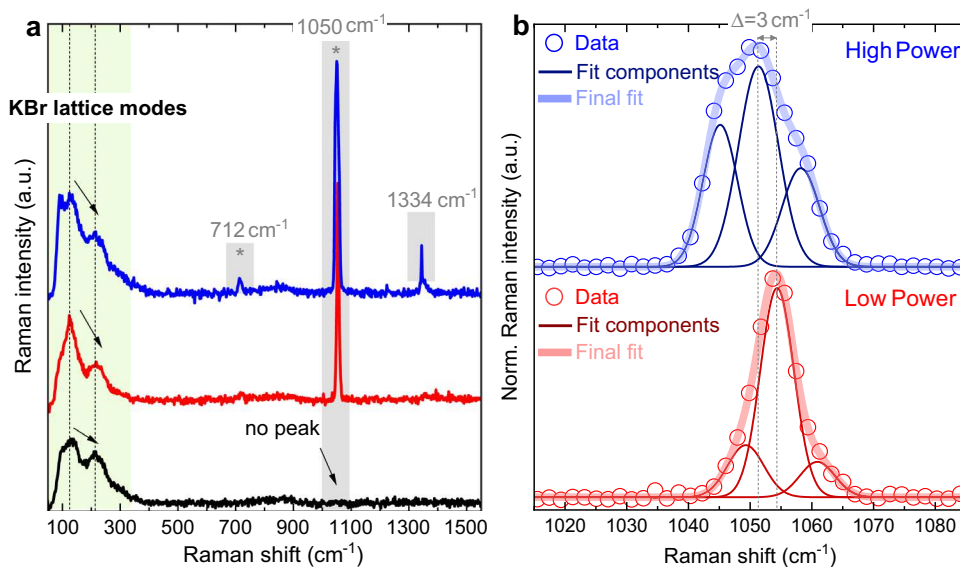
present [38]. The isotopic nitrogen ratio was further explored with ToF-SIMS.

Looking at the FTIR data in general, it could be postulated that a longer exposure of the KBr window plasma causes functionalisation of the metal halide due to the dominance of the NO_3^- anion with a small contribution of NO_2 stretching vibrations (peak 1250 cm^{-1} in Fig. 7a and XPS data for N1s in Fig. 6a). These anions could affect the vibrational properties of the KBr lattice modes at low THz frequencies which can be studied further using Raman spectroscopy.

3.5 Raman Analysis

In addition to XPS and FTIR, Raman spectroscopy was also performed on CAP-exposed KBr pellets (Fig. 9). Complementary to the mid-IR (i.e., FTIR) analysis, Raman provides an additional insight into the far-IR range where cation and anion vibrational features of KBr are accessible. In the case of a pure KBr crystal, the Raman spectrum is composed of

Fig. 9 Raman spectra of **a** untreated KBr sample, treated with low plasma power and high plasma power (480 s), and **b** accompanied by Gaussian fitting of the main NO_3^- mode



a mix of low-frequency longitudinal and transverse lattice modes (up to 9 THz or 300 cm^{-1}). The remaining spectrum, namely above 300 cm^{-1} is free of modes as expected. In contrast, both treated samples reveal a characteristic strong and narrow peak centred at about 1050 cm^{-1} that can be attributed to the NO_3^- nitrate anion stretching vibration [39]. This strong Raman mode and two additional peaks detected at 717 cm^{-1} and 1334 cm^{-1} in the high-power plasma treated sample are consistent with the previously published Raman data for KNO_3 crystals and KNO_2 structures [40–44].

The most intense NO_3^- peak was fitted (Fig. 9b) and it can be seen that the peaks obtained under low- and high-power exposure are similar but not exactly the same, with the normalised modes differing slightly in terms of the position of their maximum intensity and the contribution of the fitting components. Under high-power conditions, the maximum intensity is at 1051 cm^{-1} , which is 3 cm^{-1} lower than that observed in the lower power case. The Raman profile also has a more complex shape and is generally broader, as indicated by the contributing main and shoulder fit components. In particular, the shoulders are much larger in the high-power plasma case than in the low-power plasma case. Following data from Brooker et al. and other related articles published on the subject, this mode is attributed to A_g symmetry, with a contribution from B_{2g} symmetry and is also sensitive to the presence of defects [40, 42–44]. Moreover, the low-frequency interval ($<300\text{ cm}^{-1}$) is also modified. According to a calculated spectrum for KBr using the two-phonon frequency Born and Bradburn approach, this region consists of a mutual combination of 6 acoustic and optical frequency modes [45, 46]. After careful consideration of the spectra available, one might suspect that the intensity interplay between two intense Raman features at $120\text{--}125\text{ cm}^{-1}$ ($'A_{1g}\text{--}2E_g\text{--}T_{2g}'$ symmetry mode $\sim 3.7\text{ THz}$) and $210\text{--}215$

cm^{-1} ($'A_{1g}\text{--}E_g'$ symmetry mode $\sim 6.4\text{ THz}$) is not the same since the plasma exposes the KBr surface [46]. A peak at the higher Raman shift ($210\text{--}215\text{ cm}^{-1}$) becomes smaller, while the low-frequency peak at low power first becomes sharp and then splits, giving rise to a new component at 90 cm^{-1} previously detected in the theoretical and experimental Raman study of KNO_3 in the sub-THz region [47]. These features indicate molecular dynamics changes in the K–Br and Br–Br interactions in the cation and anion sublattices and, together with the corresponding changes in the XPS and FTIR results, provide definitive evidence for the formation of KNO_3 on the surface of KBr after plasma treatment.

3.6 ToF–SIMS Analysis

Three samples were compared by ToF–SIMS analyses, control (green), low-power: 480s (blue), and high-power: 480s (red) (Fig. 10). The mass spectra of negative secondary ions indicate that plasma treatment resulted in a significant increase in nitrate (III) and (V) concentrations on the surface compared to the reference sample [48]. Besides, NO_2^- and NO_3^- signals are also present in intense cluster ions of potassium and nitrates such as KNO_2^- , KNO_3^- , KNO_4^- , KNO_5^- , KNO_6^- , KN_2O_4^- , KN_2O_5^- and KN_2O_6^- (Fig. 10a). The presence of so many different cluster secondary ions indicates that nitrates of different oxidation states are present in high concentrations. Isotopic ratios of $^{15}\text{NO}_2^-/^{14}\text{NO}_2^-$ and $^{15}\text{NO}_3^-/^{14}\text{NO}_3^-$ (between 0.005 and 0.017) are slightly higher than their natural abundancies (0.0034) [49]. Even greater differences can be observed for the ratios of $\text{N}^{16}\text{O}^{18}\text{O}^-/\text{N}^{16}\text{O}_2^-$ and $\text{N}^{16}\text{O}_2^{18}\text{O}^-/\text{N}^{16}\text{O}_3^-$ (between 0.009 and 0.022) compared to the natural ratio of $^{18}\text{O}/^{16}\text{O}$ of 0.0019. However, this is not due to the actual isotopic enrichment but it is rather caused by the SIMS measurements.

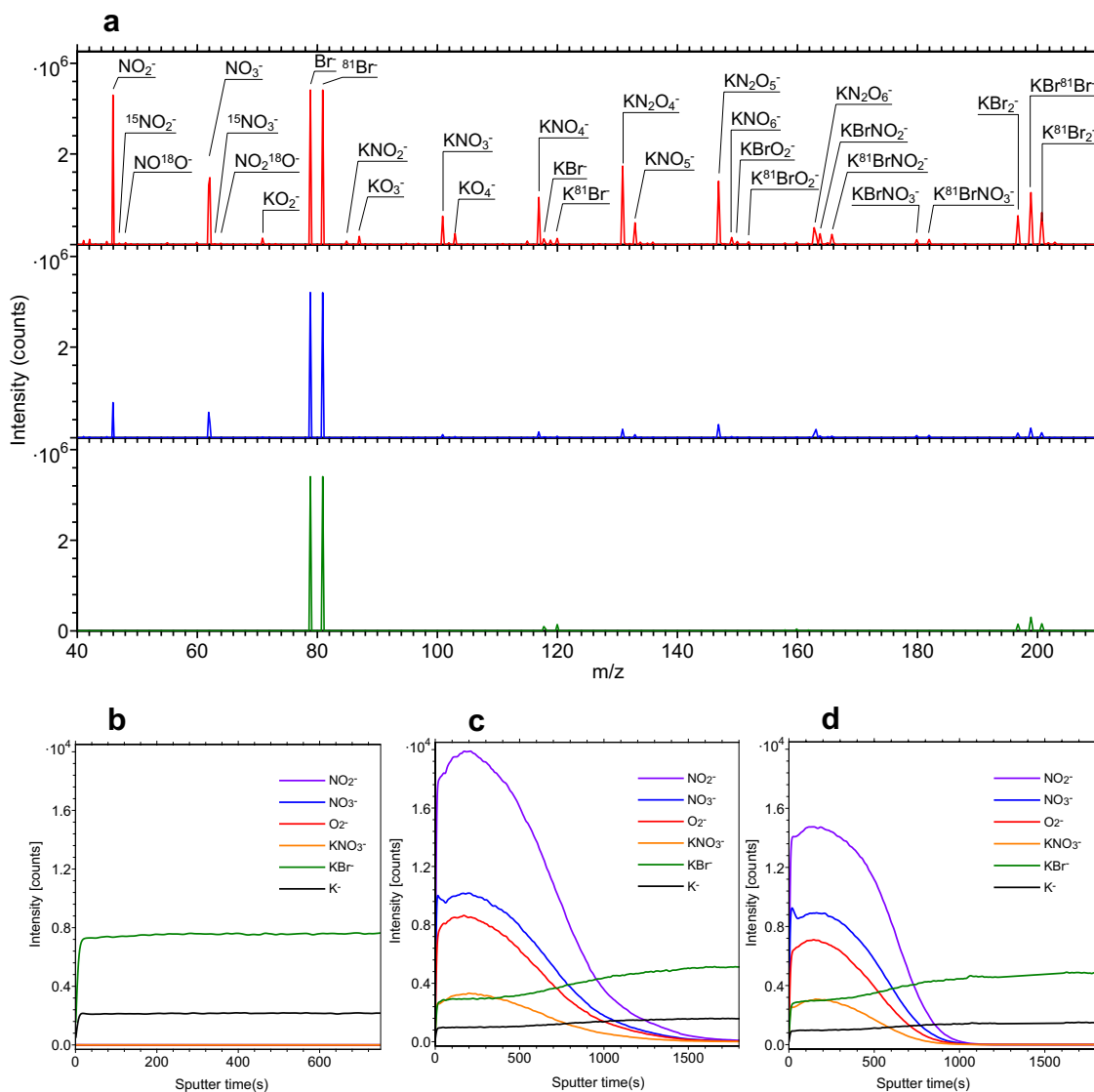


Fig. 10 **a** Survey spectra of negative secondary ions from the samples treated with high-power plasma (red), low-power plasma (blue) and untreated reference (green). Labelled are the main secondary ions on

the m/z range from 40 to 210. ToF-SIMS depth profiles of **b** control sample, **c** low-power: 480 s and **d** high-power: 480 s. Depth profiles were also measured while analysing negative secondary ions

Signals of heavier isotopes have much lower intensity so the noise of the background contributes to their intensity in relative terms much more than in case of intense signals of lighter and most abundant isotopes of N and O. Furthermore, there is also some effect of the overlapping of signals (isobaric interferences) from HNO_2^- , H_2NO_2^- , HNO_3^- and H_2NO_3^- secondary ions which have almost the same mass as nitrite and nitrate ions with heavier isotopes [50]. The occurrence of H-related fractions and heavier isotopes of oxygen (^{18}O) might alter the FTIR spectra, smearing the profile due to possible vibrational modes overlapping. The ratio of NO_2^- and NO_3^- ions compared to the KBr species is slightly higher when plasma with lower power is used, but the differences are marginal. On

the other hand, the nitrate layer on the surface is visibly thicker in the case of the treatment with the lower-power plasma (Fig. 10b). Due to the lack of an appropriate standard, it was not possible to determine the exact thickness of the nitrate layer, which is in cases of both plasma treatments between 20 and 40 nm. The control sample revealed a clean surface with negligible contamination (Fig. 10a). Considering both the FTIR and SIMS analyses, the following conclusions can be drawn: as expected, there is no isotopic separation effect caused by plasma exposure, the variations in the FTIR profile can be attributed to overlapping modes arising from a mixture of multiple species, including nitric and nitrous acids, at different durations of plasma discharge time.

4 Conclusions

This study demonstrates that FTIR gas-phase spectroscopy of the reactive oxygen and nitrogen species created by an air-based atmospheric pressure plasma can be affected by interfacial reactions at the surface of the metal halide KBr windows that form a critical element of the measurement system. The composition of reactive oxygen and nitrogen species strongly depends on the plasma generation parameters, yet, under all cases examined, were found to create an indefinite absorption region which could be considered a 'blind zone' in the range of 1300–1400 cm^{-1} . It was shown that the functionalisation is accompanied by a decrease in the atomic fraction of Br, which is replaced by the NO_3 nitrate group; the main IR absorbance peak of which progressively evolves with plasma exposure and affects the transparency of the corresponding FTIR region. The study shows a correlation between RONS and KNO_3 formation as a function of plasma power and exposure time to growth and change in molecular vibrational energies corresponding to asymmetric NO_3 stretching vibrations in the KNO_3 structure. No evidence of peak saturation was observed in real-time analysis during prolonged plasma exposure. The *in-situ* changes caused by KBr- KNO_3 transformations leading to a blind-zone cannot easily be avoided by background subtraction due to its constant and non-linear evolution during plasma exposure. In essence, this study indicates that the absorption region resulting from KNO_3 formation on the surface of KBr windows during plasma exposure must be taken into account when attempting to quantify important gas phase RONS, such as HNO_2 and HNO_3 , with absorption peaks in the 1300–1400 cm^{-1} .

Acknowledgements The authors gratefully acknowledge financial support from the Public Agency for Research Activity of the Republic of Slovenia (awards J2-4490, J2-4451 and L2-4481), the UK Engineering and Physical Sciences Research Council (EPSRC) (awards EP/S025790/1 and EP/N021347/1) and NATO (award G5814).

Data availability The data is available upon reasonable request.

Declarations

Conflict of interest The authors declare that they have no conflicts of interest.

Open Access This article is licensed under a Creative Commons Attribution 4.0 International License, which permits use, sharing, adaptation, distribution and reproduction in any medium or format, as long as you give appropriate credit to the original author(s) and the source, provide a link to the Creative Commons licence, and indicate if changes were made. The images or other third party material in this article are included in the article's Creative Commons licence, unless indicated otherwise in a credit line to the material. If material is not included in the article's Creative Commons licence and your intended use is not permitted by statutory regulation or exceeds the permitted use, you will

need to obtain permission directly from the copyright holder. To view a copy of this licence, visit <http://creativecommons.org/licenses/by/4.0/>.

References

1. Waskow A, Ibba L, Leftley M, Howling A, Ambrico PF, Furno I. An *in situ* FTIR study of DBD plasma parameters for accelerated germination of *Arabidopsis thaliana* seeds. *Int J Mol Sci*. 2021;22(21):11540.
2. Katsigiannis AS, Bayliss DL, Walsh JL. Cold plasma for the disinfection of industrial food-contact surfaces: an overview of current status and opportunities. *Compr Rev Food Sci Food Saf*. 2022;21(2):1086–124.
3. Hojnik N, Modic M, Tavčar-Kalcher G, Babič J, Walsh JL, Cvelbar U. Mycotoxin decontamination efficacy of atmospheric pressure air plasma. *Toxins (Basel)*. 2019;11(4):219.
4. Hong J, Yick S, Chow E, Murdock A, Fang J, Seo DH, Wolff A, Han Z, van der Laan T, Bendavid A, Ostrikov K, Murphy AB. Direct plasma printing of nano-gold from an inorganic precursor. *J Mater Chem C Mater*. 2019;7(21):6369–74.
5. Shvalya V, Vasudevan A, Modic M, Abutoama M, Skubic C, Nadižar N, Zavašnik J, Vengust D, Zidanšek A, Abdulhalim I, Rozman D, Cvelbar U. Bacterial DNA recognition by SERS active plasma-coupled nanogold. *Nano Lett*. 2022;22(23):9757–65.
6. Liu F, Nie L, Lu X, Stephens J, Ostrikov K. Atmospheric plasma VUV photon emission. *Plasma Sources Sci Technol*. 2020;29(6):065001.
7. Reuter S, Sousa JS, Stancu GD, Hubertus van Helden J-P. Review on VUV to MIR absorption spectroscopy of atmospheric pressure plasma jets. *Plasma Sources Sci Technol*. 2015;24(5):054001.
8. van Hest MFAM, de Graaf A, van de Sanden MCM, van Hest MFAM, de Graaf A, Schram DC. Use of *in situ* FTIR spectroscopy and mass spectrometry in an expanding hydrocarbon plasma. *Plasma Sources Sci Technol*. 2000;9(4):615–24.
9. Riccardi C, Barni R. Chemical kinetics in air plasmas at atmospheric pressure. In: *Chemical kinetics*. London: InTech; 2012. p. 185–202.
10. Sakiyama Y, Graves DB, Chang HW, Shimizu T, Morfill GE. Plasma chemistry model of surface microdischarge in humid air and dynamics of reactive neutral species. *J Phys D Appl Phys*. 2012;45(42):425201.
11. Harris DC. Materials for infrared windows and domes: properties and performance. In: *SPIE 1999*
12. Sivachandiran L, Khacef A. Enhanced seed germination and plant growth by atmospheric pressure cold air plasma: combined effect of seed and water treatment. *RSC Adv*. 2017;7(4):1822–32.
13. Reuter S, Winter J, Iseni S, Schmidt-Bleker A, Dunnbier M, Masur K, Wende K, Weltmann K-D. The influence of feed gas humidity versus ambient humidity on atmospheric pressure plasma jet-effluent chemistry and skin cell viability. *IEEE Trans Plasma Sci*. 2015;43(9):3185–92.
14. Jo J-O, Lee SB, Jang DL, Mok YS. Plasma-catalytic ceramic membrane reactor for volatile organic compound control. *IEEE Trans Plasma Sci*. 2013;41(10):3021–9.
15. Gershman S, Fetsch H, Gorky F, Carreon ML. Identifying regimes during plasma catalytic ammonia synthesis. *Plasma Chem Plasma Process*. 2022;42(4):731–57.
16. Pavlovich MJ, Clark DS, Graves DB. Quantification of air plasma chemistry for surface disinfection. *Plasma Sources Sci Technol*. 2014;23(6): 065036.

17. Shimizu T, Sakiyama Y, Graves DB, Zimmermann JL, Morfill GE. The dynamics of ozone generation and mode transition in air surface micro-discharge plasma at atmospheric pressure. *New J Phys.* 2012;14(10): 103028.
18. Hojnik N, Modic M, Žigon D, Kovač J, Jurov A, Dickenson A, Walsh JL, Cvelbar U. Cold atmospheric pressure plasma-assisted removal of aflatoxin B₁ from contaminated corn kernels. *Plasma Process Polym.* 2021;18(1):2000163.
19. Modic M, McLeod NP, Sutton JM, Walsh JL. Cold atmospheric pressure plasma elimination of clinically important single- and mixed-species biofilms. *Int J Antimicrob Agents.* 2017;49(3):375–8.
20. Modic M, Kovač J, Nicholls JR, Kos Š, Serša G, Cvelbar U, Walsh JL. Targeted plasma functionalization of Titanium inhibits polymicrobial biofilm recolonization and stimulates cell function. *Appl Surf Sci.* 2019;487:1176–88.
21. Hojnik N, Modic M, Walsh JL, Žigon D, Javornik U, Plavec J, Žegura B, Filipič M, Cvelbar U. Unravelling the pathways of air plasma induced aflatoxin B₁ degradation and detoxification. *J Hazard Mater.* 2021;403:123593.
22. Suhadolnik L, Bele M, Čekada M, Jovanovič P, Maselj N, Lončar A, Dražič G, Šala M, Hodnik N, Kovač J, Montini T, Melchionna M, Fornasiero P. Nanotubular TiO_x N_y-supported Ir single atoms and clusters as thin-film electrocatalysts for oxygen evolution in acid media. *Chem Mater.* 2023;35(6):2612–23.
23. Stanfield SA, Menart J, DeJoseph C, Kimmel RL, Hayes JR. Rotational and vibrational temperature distributions for a dielectric barrier discharge in air. *AIAA J.* 2009;47(5):1107–15.
24. Hasan MI, Walsh JL. Numerical investigation of the spatiotemporal distribution of chemical species in an atmospheric surface barrier-discharge. *J Appl Phys.* 2016;119(20): 203302.
25. Kramida A, Ralchenko Yu, Reader J, NIST ASD Team (2022) NIST Atomic Spectra Database (version 5.10), [Online]. Available: <https://physics.nist.gov/asd> [Sun Dec 03 2023]. National Institute of Standards and Technology, Gaithersburg, MD. <https://doi.org/10.18434/T4W30F>
26. Alexander V, Naumkin AK-VSWG and CJP. NIST X-ray photoelectron spectroscopy database, NIST standard reference database number 20, National Institute of Standards and Technology, Gaithersburg MD, 20899 (2000).
27. Crist BV. KBr crystal: cleaved in air. *Surf Sci Spectra.* 1992;1(3):292–6.
28. Baltrusaitis J, Jayaweera PM, Grassian VH. XPS study of nitrogen dioxide adsorption on metal oxide particle surfaces under different environmental conditions. *Phys Chem Chem Phys.* 2009;11(37):8295.
29. Rosseler O, Sleiman M, Montesinos VN, Shavorskiy A, Keller V, Keller N, Litter MI, Bluhm H, Salmeron M, Destaillets H. Chemistry of NO_x on TiO₂ surfaces studied by ambient pressure XPS: products, effect of UV irradiation, water, and coadsorbed K⁺. *J Phys Chem Lett.* 2013;4(3):536–41.
30. Jones WD, Marx KA, Croft S. Infrared intensities of the nitrite ion in solid solution in potassium bromide. *J Mol Spectrosc.* 1969;30(1–3):498–505.
31. Kato R, Rolfe J. Vibration frequencies of NO₂⁻ and NO₃⁻ Ions in KBr crystals. *J Chem Phys.* 1967;47(6):1901–10.
32. Yeung LY, Li S, Kohl IE, Haslun JA, Ostrom NE, Hu H, Fischer TP, Schauble EA, Young ED. Extreme enrichment in atmospheric ¹⁵N ¹⁵N. *Sci Adv.* 2017;3(11):6741.
33. Forney D, Thompson WE, Jacox ME. The vibrational spectra of molecular ions isolated in solid neon. XI. NO²⁺, NO²⁻, and NO³⁻. *J Chem Phys.* 1993;99(10):7393–403.
34. Guillory WA, Bernstein ML. Infrared spectrum of matrix-isolated nitric acid. *J Chem Phys.* 1975;62(3):1058–60.
35. Chen W-J, Lo W-J, Cheng B-M, Lee Y-P. Photolysis of nitric acid in solid nitrogen. *J Chem Phys.* 1992;97(10):7167–73.
36. Nakamoto K, Fujita J, Murata H. Infrared spectra of metallic complexes. V. The infrared spectra of nitro and nitrito complexes. *J Am Chem Soc.* 1958;80(18):4817–23.
37. Falk M. Infrared spectrometric determination of nitrate, nitrite and ammonium ions by means of matrix isolation in pressed alkali metal halide pellets. *Vib Spectrosc.* 1990;1(1):69–79.
38. Mochida M, Finlayson-Pitts BJ. FTIR studies of the reaction of gaseous NO with HNO₃ on porous glass: implications for conversion of HNO₃ to photochemically active NO_x in the atmosphere. *J Phys Chem A.* 2000;104(43):9705–11.
39. Fontana MD, Ben Mabrouk K, Kauffmann TH. Raman spectroscopic sensors for inorganic salts. Spectroscopic properties of inorganic and organometallic compounds. *R Soc Chem.* 2013;44:40–67.
40. Brooker MH. Raman study of the structural properties of KNO₃(II). *Can J Chem.* 1977;55(7):1242–50.
41. Acosta-Maeda TE, Misra AK, Muzangwa LG, Berlanga G, Muchow D, Porter J, Sharma SK. Remote Raman measurements of minerals, organics, and inorganics at 430 m range. *Appl Opt.* 2016;55(36):10283.
42. Brooker MH, Irish DE. Infrared and Raman spectral studies of KNO₂–KNO₃ solutions. *Can J Chem.* 1968;46(2):229–33.
43. Liu D, Ullman FG, Hardy JR. Raman scattering and lattice-dynamical calculations of crystalline KNO₃. *Phys Rev B.* 1992;45(5):2142–7.
44. Akiyama K, Morioka Y, Nakagawa I. Raman and infrared spectra and lattice vibrations of KNO₃ crystal. *J Phys Soc Jpn.* 1980;48(3):898–905.
45. Ghomi M, Buisson JP. Study of Raman spectra of KBr doped with F-centres by excitation in the F and K bands. *J Phys C Solid State Phys.* 1979;12(21):4631–40.
46. Pasternak A, Cohen E, Gilat G. Calculation of second-order Raman scattering for KBr, NaCl, and MgO crystals. *Phys Rev B.* 1974;9(10):4584–92.
47. Mohammad MR, Sherman WF. Infrared and Raman spectra of alkali halide/NO₃⁻ systems. *J Mol Struct.* 1984;115(C):217–20.
48. Fichtner M, Goschnick J, Ache HJ. Identification of nitrates and sulphates with dynamic SIMS. *Fresenius J Anal Chem.* 1994;348(3):201–4.
49. Haneda H, Ohgaki T, Sakaguchi I, Ryoken H, Ohashi N, Yasumori A. SIMS analysis of impurities and nitrogen isotopes in gallium nitride thin films. *Appl Surf Sci.* 2006;252(19):7265–8.
50. Petts DC, Chacko T, Stachel T, Stern RA, Heaman LM. A nitrogen isotope fractionation factor between diamond and its parental fluid derived from detailed SIMS analysis of a gem diamond and theoretical calculations. *Chem Geol.* 2015;410:188–200.